Interplay between Defect Propagation and Surface Hydrogen in Silicon Nanowire Kinking Superstructures

Naechul Shin,[†] Miaofang Chi,[‡] and Michael A. Filler*,[†]

[†]School of Chemical & Biomolecular Engineering, Georgia Institute of Technology, Atlanta, Georgia 30332, United States, and [‡]Materials Science & Technology Division, Oak Ridge National Laboratory, Oak Ridge, Tennessee 37831, United States

ABSTRACT Semiconductor nanowire kinking superstructures, particularly those with long-range structural coherence, remain difficult to fabricate. Here, we combine high-resolution electron microscopy with *operando* infrared spectroscopy to show why this is the case for Si nanowires and, in doing so, reveal the interplay between defect propagation and surface chemistry during ⟨211⟩ → ⟨111⟩ and ⟨211⟩ → ⟨211⟩ kinking. Our experiments show that adsorbed hydrogen atoms are responsible for selecting ⟨211⟩-oriented growth and indicate that a twin boundary imparts structural coherence. The twin boundary, only continuous at ⟨211⟩ → ⟨211⟩ kinks, reduces the symmetry of the trijunction and limits the number of degenerate directions available to the nanowire. These findings constitute a general approach for rationally engineering kinking superstructures and also provide important insight into the role of surface chemical bonding during vapor–liquid–solid synthesis.

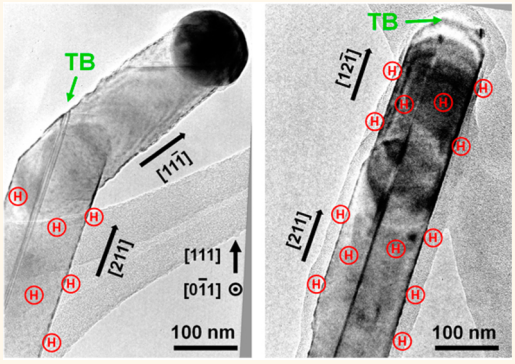

KEYWORDS: silicon · nanowire · kinking · defects · surface · hydrogen

Semiconductor nanowires containing kinking superstructures—multiple, user-programmable changes to growth orientation—offer tantalizing opportunities to fabricate nanoelectronic bioprobes,[1−3] generate metamaterials with chiroptical response,[4] reduce thermal conductivity,[5] and explore nanomechanical behavior.[6] While the synthesis of such structures is possible *via* shape-guided lateral growth[7] or metal-assisted chemical etching,[8] the vapor–liquid–solid (VLS) technique holds particular promise.[9,10] For example, VLS allows for the integration of additional functionality *via* selective doping[11] and/or heterostructure formation.[12]

The point where a nanowire changes its growth orientation—the "kink"—is the most basic building block of any kinking superstructure. Si nanowires frequently exhibit ⟨111⟩ → ⟨211⟩ kinks at low temperatures,[13] at high pressures,[14−16] and/or upon the addition of hydrogen on the sidewall.[17] More recently, ⟨111⟩ → ⟨110⟩ and ⟨100⟩ → ⟨111⟩ kinks have been demonstrated for Ge and InP nanowires, respectively.[10,18] However, crystal symmetry generally precludes the selection of a specific crystal orientation (*e.g.*, [211]) when many degenerate options (*e.g.*, [121], [112], *etc.*) are available.

The demonstration of ⟨211⟩/⟨211⟩ kinking superstructures reveals that structural coherence is, in fact, possible. A series of ⟨211⟩ → ⟨211⟩ kinks, each attainable with a brief pressure decrease, yields structures consisting only of segments oriented in a small subset of degenerate crystal directions.[1,9] Identification of the chemical and structural details responsible for this behavior, which occurs despite the high degree of symmetry in the diamond cubic lattice, would represent an important step toward the *ab initio* design of kinking superstructures. Structural motifs that break the symmetry of the nanowire growth interface are a logical explanation for kinking superstructure coherence. While planar defects, particularly twin boundaries (TB)[19−21] and/or polytypes,[22,23] often coincide with ⟨211⟩-oriented growth in Si nanowires, their influence on Si nanowire kinking superstructure synthesis is unknown.[1,9]

* Address correspondence to michael.filler@chbe.gatech.edu.

Received for review January 29, 2014 and accepted March 7, 2014.

Published online March 07, 2014
10.1021/nn500598d

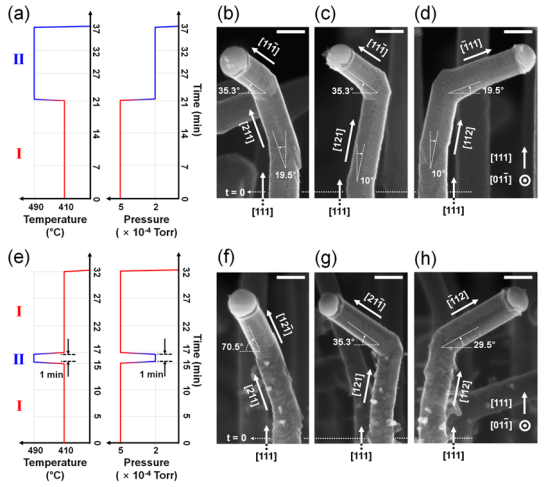

Figure 1. Multiple degenerate kink directions. (a) Schematic profile of substrate temperature and Si_2H_6 pressure as a function of time for ⟨211⟩ → ⟨111⟩ kinking. Condition I: 5×10^{-4} Torr Si_2H_6 and 410 °C. Condition II: 2×10^{-4} Torr Si_2H_6 and 490 °C. Side view SEM images along the [01$\bar{1}$] direction of representative Si nanowires showing ⟨211⟩ → ⟨111⟩ kinking: (b) [211] → [11$\bar{1}$], (c) [121] → [11$\bar{1}$], and (d) [112] → [$\bar{1}$11]. Scale bars, 100 nm. (e) Schematic profile of Si_2H_6 pressure and substrate temperature as a function of time for ⟨211⟩ → ⟨211⟩ kinking. Side view SEM images along the [0$\bar{1}$1] direction of representative Si nanowires showing ⟨211⟩ → ⟨211⟩ kinking: (f) [211] → [12$\bar{1}$], (g) [121] → [21$\bar{1}$], and (h) [112] → [$\bar{1}$12]. Scale bars, 100 nm. For both kink types, substrate-attached [111] segments exist at the base of these nanowires and are grown for 10 min under condition II. The axial positions where condition I is initially applied, and corresponding to t = 0, are indicated with white dotted lines at the bottom of each SEM image.

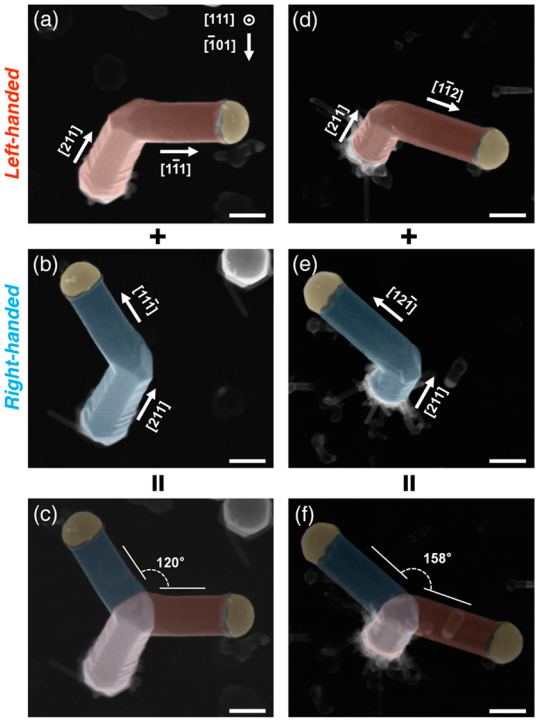

Figure 2. Left- and right-handed superstructures. Top view SEM images of representative (a) [211] → [1$\bar{1}$1] (false-colored red) and (b) [211] → [11$\bar{1}$] (false-colored blue) kinks. (c) Superimposition of the kinks in (a) and (b). Top view SEM images of representative (d) [211] → [1$\bar{1}$2] (false-colored red) and (e) [211] → [12$\bar{1}$] (false-colored blue) kinks. (f) Superimposition of the kinks shown in (d) and (e). Scale bars, 100 nm. The initial, substrate-attached [111] segment is hidden from view in all images.

Here, we advance the understanding of Si nanowire kinking superstructure synthesis by revealing the subtle, yet critical, interplay between growth orientation, defect propagation, and surface chemistry. We show that a continuous TB is present only at ⟨211⟩ → ⟨211⟩ kinks and explain its role in coherent superstructure formation. In particular, the nucleation pinning that accompanies the TB forces the nanowire to select from two, as opposed to the many possible, ⟨211⟩ directions at each kink. Despite the favorability of nucleation at the TBs present in ⟨211⟩ nanowires,[20,21,23,24] we also find that adsorbed hydrogen atoms are predominantly responsible for driving ⟨211⟩ growth. Removal of hydrogen returns the nanowire to ⟨111⟩ growth and results in TB termination at the sidewall.

RESULTS AND DISCUSSION

Two types of kink are shown in Figure 1, ⟨211⟩ → ⟨111⟩ and ⟨211⟩ → ⟨211⟩, and reveal, similar to our previous work[17] as well as that of others,[13−16] the relationship between Si nanowire growth direction and synthesis conditions. After growth of the initial substrate-attached [111] segment and as illustrated in Figure 1a, we generate ⟨211⟩ → ⟨111⟩ kinks by growing with condition I and then transitioning to condition II. Figure 1b−d show representative side view SEM images measured along the [01$\bar{1}$] direction of the resulting kinks. The observed intersegment angles are consistent with that expected between ⟨211⟩ and ⟨111⟩ segments when projected onto the (01$\bar{1}$) plane (Supporting Information, Figure S1). We provide TEM confirmation of these growth orientation assignments below. The generation of ⟨211⟩ → ⟨211⟩ kinks, as illustrated in Figure 1e, is accomplished by starting with condition I, briefly transitioning to condition II (for 1 min), and subsequently returning to condition I. Side view SEM images measured along the [01$\bar{1}$] direction of representative Si nanowires containing ⟨211⟩ → ⟨211⟩ kinks are displayed in Figure 1f−h. The observed intersegment angles are clearly distinct from those for ⟨211⟩ → ⟨111⟩ kinks (Figure 1b−d) and provide initial confirmation of ⟨211⟩ → ⟨211⟩ kinking (Supporting Information, Figure S1). In this case, we observe small-diameter nanowires on the sidewalls of the first ⟨211⟩ segment and attribute their presence to Au diffusion and subsequent nucleation on the sidewall.[17,25]

Figure 2 shows top-down SEM images of representative nanowires containing ⟨211⟩ → ⟨111⟩ and ⟨211⟩ → ⟨211⟩ kinks and highlights the chirality of individual nanowires. When viewing nanowires in this manner, the substrate-attached [111] segment is hidden. Here, we label the first ⟨211⟩ segment as [211], no matter its specific crystallographic direction (*i.e.*, [211], [121],

or [112]), and name subsequent segments accordingly. This simplified nomenclature is particularly useful when discussing TEM images (*vida infra*) since different, yet degenerate crystallographic directions can appear identical when projected into the plane. Figure 2a and b show nanowires that kink from [211] to one of two degenerate ⟨111⟩ directions (*i.e.*, [1$\bar{1}$1] or [11$\bar{1}$]). The overall nanowire, assuming the substrate-attached [111] segment defines the axis of rotation, is chiral and exhibits either left (false-colored in red) or right (false-colored blue) handedness. Analogous SEM images of left- and right-handed nanowires containing [211] → ⟨211⟩ kinks are displayed in Figure 2d and e. By overlaying the SEM images of left- and right-handed nanowires, as shown in Figure 2c and f, we observe angles of 120° and 158°, as expected for two final ⟨111⟩ and ⟨211⟩ segments, respectively, when viewed in this direction (Supporting Information, Figure S1). Notably, Figure 2 shows only two of the six structures observed for each kink type (Supporting Information, Figure S2). Such a large number of crystallographically degenerate structures suggests that highly coherent superstructures are unlikely, a point we return to below.

We now analyze the crystal structure of, and propagation of defects in, [211] → ⟨111⟩ and [211] → ⟨211⟩ kinks *via* the TEM images in Figures 3a−c and 3d−f, respectively. The initial and final segments for both kink types, as labeled in the low-magnification images of Figure 3a and d, are based on the high-resolution TEM (HRTEM) images in Figure 3b,c and e,f, respectively. The initial [211] segment, which is identical for and located immediately prior to both kink types, exhibits four {113} sidewalls and two {111} sidewalls (Supporting Information, Figure S3). We note that small {110} sidewalls[26,27] are not clearly observed for our nanowires. Most importantly, an axially oriented TB is present and intersects with the edge between the two {111} planes comprising the liquid-solid interface of the [211] segment (Supporting Information, Figure S3).[19,22]

Figure 3b displays a HRTEM image measured along the [2$\bar{3}$1] zone axis[28] at the [211] → ⟨111⟩ kink that exhibits two sets of Si(111) lattice fringes. These fringes, rotated ~126° with respect to each other, combined with the presence of a forbidden 1/3 [422] reflection in the fast Fourier transform (FFT) pattern inset of Figure 3b, suggest that the lattice is not single-crystalline diamond cubic.[29] Despite recent reports of hexagonal Si nanowires,[30,31] the fringe rotation angle seen here and data discussed below indicate that this pattern is the consequence of a ($\bar{1}$11) TB oriented ~68° relative to the [2$\bar{3}$1] zone axis.[28,29,32] The twinned and untwinned lattices share the same diffraction spot, specifically [422], as highlighted with a red circle. The HRTEM image in Figure 3c, in conjunction with the FFT pattern inset recorded beyond the kink (*i.e.*, closer to the nanowire tip), confirms that the final segment is

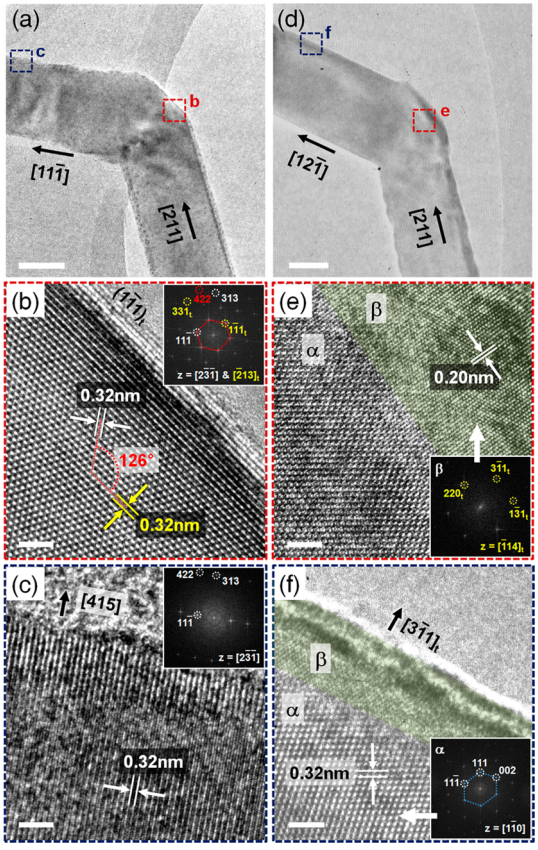

Figure 3. Kink crystal structure analysis. (a) Low-magnification TEM image of a representative [211] → [11$\bar{1}$] kink. Scale bar, 50 nm. (b, c) High-resolution TEM images of the regions denoted by the dotted boxes in (a). Scale bars, 2 nm. Insets are FFT diffraction patterns of each TEM image. (d) Low-magnification TEM image of a representative [211] → [12$\bar{1}$] kink. Scale bar, 50 nm. (e, f) High-resolution TEM images of the regions denoted by the dotted boxes in (d). Scale bars, 2 nm. Two distinct lattices, denoted α and *β*, can be seen in (e) and (f). The *β* region is false-colored green for clarity. The FFT pattern insets in (e) and (f) are of the *β* and α's, respectively.

indeed single-crystalline diamond cubic phase and [11$\bar{1}$] oriented. The direction of the [422] spot is identical to that of the [211] segment in Figure 3a and confirms that the [211] and [11$\bar{1}$] segments lie in the (2$\bar{3}$1) plane. The data in Figure 3b and c provide initial evidence that the TB terminates shortly after the [211] → [11$\bar{1}$] kink.

Figure 3e and f show HRTEM images of a [211] → ⟨211⟩ kink. Two crystal lattices, labeled α and *β*, are observed both at and beyond the kink. The FFT patterns in the Figure 3e and f insets reveal that the zone axes of the *β* and α lattices are [$\bar{1}$14]$_t$ (where t denotes the twinned lattice) and [1$\bar{1}$0], respectively, and confirm that the final segment is [12$\bar{1}$] oriented. Since a [1$\bar{1}$0] zone axis converts to [$\bar{1}$14] *via* a Householder reflection with respect to the ($\bar{1}$11) plane[33] which is identical to the plane occupied by the TB, the α and *β* lattices exhibit a twinned relationship. Unlike the [211] → [11$\bar{1}$] kink, where the TB appears to terminate, the presence of two lattices (*i.e.*, α and *β*) at and beyond a [211] → [12$\bar{1}$] kink indicates that the

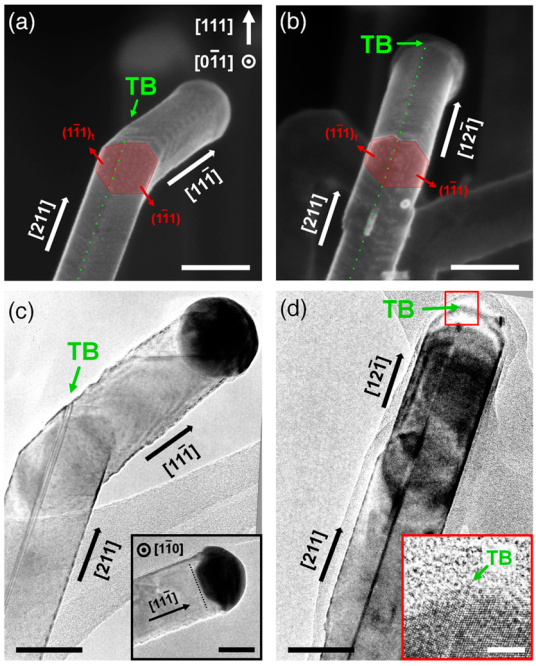

Figure 4. Differences in TB propagation. Side view SEM images along the [0$\bar{1}$1] direction of representative (a) [211] → [11$\bar{1}$] and (b) [211] → [12$\bar{1}$] kinks. The approximate location of each TB is denoted by green dotted lines and arrows. Important sidewall facets are false-colored in red. Scale bars, 100 nm. (c) Bright-field TEM image along the [0$\bar{1}$1] zone axis of a representative [211] → [11$\bar{1}$] kink showing that the TB terminates at the sidewall of the [11$\bar{1}$] segment. Scale bar, 50 nm. Inset: Bright-field TEM image of the catalyst droplet showing the main liquid−solid interface is (11$\bar{1}$)$_{SL}$ in the final [11$\bar{1}$] segment. Scale bar, 20 nm. (d) Bright-field TEM image along the [0$\bar{1}$1] zone axis of a representative [211] → [12$\bar{1}$] kink. The TB does not terminate in this situation, but propagates inside the new [12$\bar{1}$] segment. Scale bar, 50 nm. Inset: High-resolution TEM image showing the TB at, and inverted faceting of, the liquid−solid interface. Scale bar, 5 nm.

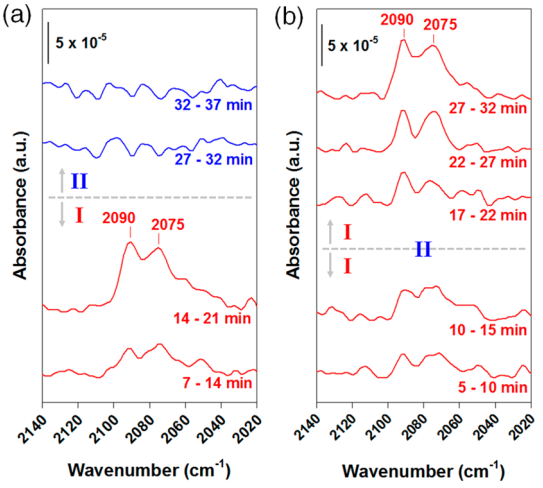

Figure 5. Hydrogen termination as a function of growth direction. (a) *Operando* infrared spectra of the ν(Si−H) stretching region measured before and after ⟨211⟩ → ⟨111⟩ kink formation. The gray dotted line, located between the 14−21 and 27−32 min spectra, denotes the transition between conditions I and II (Figure 1a). Since Si_2H_6 pressure and substrate temperature change at this point, a new background spectrum is recorded at 22−27 min. (b) *Operando* infrared spectra of the ν(Si−H) stretching region measured before and after ⟨211⟩ → ⟨211⟩ kink formation. The gray dotted line, located between the 10−15 and 17−22 min spectra, marks the 1 min step at condition II prior to returning to condition I (Figure 1e).

TB continues to propagate. In addition, the sidewall orientation of the β lattice in the [12$\bar{1}$] segment is identified as [3$\bar{1}$1]$_t$ in Figure 3f and corroborates the presence of {113} sidewalls in ⟨211⟩ segments (Supporting Information, Figure S3).

We verify the presence and propagation behavior of the TB at [211] → [11$\bar{1}$] and [211] → [12$\bar{1}$] kinks *via* the SEM and TEM images measured along the [0$\bar{1}$1] direction in Figure 4. As anticipated from the above discussion, Figure 4c shows that the ($\bar{1}$11) TB present in the [211] segment terminates at the sidewall of the [11$\bar{1}$] segment following a [211] → [11$\bar{1}$] kink. While two {111} facets comprise the liquid−solid interface during [211] segment growth (Supporting Information, Figure S3), the Figure 4c inset also shows that the main liquid−solid facet reverts to (11$\bar{1}$)$_{SL}$ (where SL denotes the liquid−solid interface). Importantly, Figure 4d confirms that the TB is continuous at [211] → [12$\bar{1}$] kinks and, as seen in the HRTEM inset, extends to the growth front. Crystallography requires that the [12$\bar{1}$] segment liquid−solid interface be inverted relative to the first [211] segment (Supporting Information, Figure S4). Thus, the liquid−solid interface of the [12$\bar{1}$] segment will consist of (11$\bar{1}$)$_{SL}$ and (11$\bar{1}$)$_{SL,t}$ facets that intersect with an angle of 219°. We are able to identify a signature of this inversion (Supporting Information, Figure S5) and expect it to occur at each successive ⟨211⟩ → ⟨211⟩ kink.

Figure 5 displays *operando* infrared absorption spectra for arrays of nanowires containing either ⟨211⟩ → ⟨111⟩ or ⟨211⟩ → ⟨211⟩ kinks. Here, we revert to labeling growth orientations as families of directions since the infrared beam is sampling an ensemble of nanowires. Our prior infrared study of the Au/Si system shows that absorption peak intensity linearly correlates with hydrogen atom surface coverage over the same range of growth conditions utilized here.[17] Spectra of the ν(Si−H) stretching region recorded before (*i.e.*, condition I, 7−14 and 14−21 min) and after (*i.e.*, condition II, 27−32 and 32−37 min) ⟨211⟩ → ⟨111⟩ kinking is shown in Figure 5a. Two characteristic peaks at 2075 and 2090 cm^{-1} increase in intensity during ⟨211⟩ segment growth. Consistent with the {111} and {113} facets observed for ⟨211⟩-oriented nanowires (Supporting Information, Figure S3) and our prior work,[17] we assign these features to hydrogen adsorbed as monohydride on {111} and {113} facets. Spectra measured during ⟨111⟩ segment growth following the ⟨211⟩ → ⟨111⟩ kink reveal that ν(Si−H) modes, and thus adsorbed hydrogen atoms, are no longer present. Figure 5b shows analogous *operando* infrared spectra recorded before (*i.e.*, condition I, 5−10 and 10−15 min) and

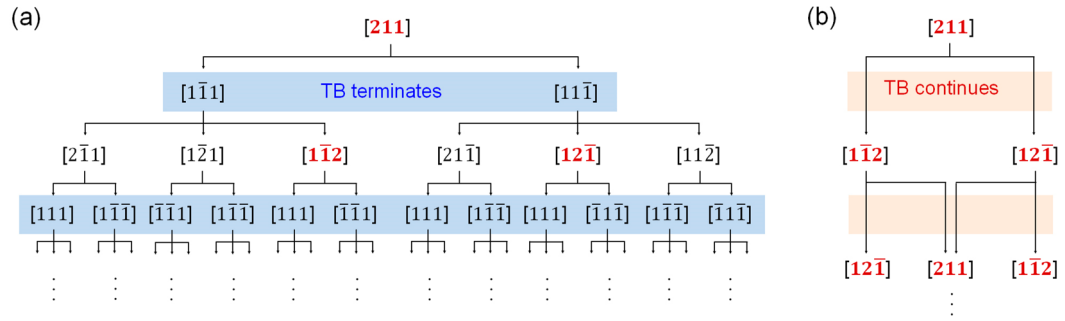

Figure 6. Kinking superstructure decision trees. (a) If the TB terminates, as is the case at a [211] → [1$\bar{1}$1] or [11$\bar{1}$] kink, the next segment can select from any of three degenerate ⟨211⟩ directions. Two segments after the original [211] segment, there are now six possible ⟨211⟩ available to the nanowire, and superstructure coherence will be low. (b) The continuation of the TB at [211] → [1$\bar{1}$2] or [12$\bar{1}$] kinks forces the nanowire to select from one of two directions, which are angled 120° with respect to each other and coplanar with the TB. This situation leads to highly coherent superstructures.

after (*i.e.*, condition I, 17−22, 22−27, and 27−32 min) ⟨211⟩ → ⟨211⟩ kinking. During growth of the first ⟨211⟩ segment, and similar to that observed for the 7−14 and 14−21 min time points in Figure 5a, the ν(Si−H) stretching mode intensity increases. These features are again attributed to hydrogen atoms adsorbed on {111} and {113} facets. Growth of the second ⟨211⟩ segment results in a further increase of these modes, indicating that adsorbed hydrogen remains. We are not able to directly probe the hydrogen coverage during the 1 min application of condition II, but expect that some, if not all, of the hydrogen is temporarily removed *via* H_2 desorption.[34]

We propose a mechanism for [211] → ⟨111⟩ and [211] → ⟨211⟩ kinking based on our observations of growth direction, TB propagation, and adsorbed hydrogen. Higher Si_2H_6 pressures and lower substrate temperatures, which are present under condition I, result in the growth of hydrogen-terminated and TB-containing [211] segments. When applying condition II, which occurs at the initiation of both kink types and favors ⟨111⟩-oriented growth, hydrogen desorption accelerates and {111} facets, specifically (1$\bar{1}$1) and $(1\bar{1}1)_t$, emerge from the {113} facets (Supporting Information, Figure S6). The catalyst droplet will eventually wet the opposing sidewall facets.[35] The mechanisms for [211] → ⟨111⟩ and [211] → ⟨211⟩ kinking diverge beyond this point as a result of continuing growth with condition II or by reverting to condition I, respectively. For a ⟨211⟩ → ⟨111⟩ kink, the $(11\bar{1})_{SL,t}$ facet shrinks and the main liquid−solid facet becomes strictly $(11\bar{1})_{SL}$. The TB is now propagating at a 19.5° angle relative to the new ⟨111⟩ growth direction, eventually meeting with and terminating at the nanowire sidewall (Figure 4c). The situation is distinct for ⟨211⟩ → ⟨211⟩ kinking. Since condition II, which favors ⟨211⟩ growth, is applied after 1 min, the TB is not able to reach the nanowire sidewall, and it continues to propagate along the new [12$\bar{1}$] growth direction (Figure 4d). During this process, the $(111)_{SL,t}$ and $(111)_{SL}$ transition to $(11\bar{1})_{SL,t}$ and $(11\bar{1})_{SL}$.

The termination or continuation of a symmetry-breaking structural motif, such as the TB observed here, explains the relative difficulty or ease of creating coherently kinked superstructures, respectively.[9] When the TB terminates at a [211] → [1$\bar{1}$1] or [11$\bar{1}$] kink (or a [211] → ⟨211⟩ kink with a sufficiently long step at condition II), nucleation returns to the truncated facets on the {112} sidewalls.[36,37] The addition of another ⟨211⟩ segment then requires the generation of a new TB, which can emerge from any of the broad {112} sidewalls. Superstructure coherence is lost in this situation, as Figure 6a illustrates, since the new ⟨211⟩ segment can propagate in any of *three* possible directions (*i.e.*, [2$\bar{1}$1], [1$\bar{2}$1], or [1$\bar{1}$2] for a preceding [1$\bar{1}$1] segment). However, the continuous TB present in the case of [211]-oriented growth forces nucleation to occur at or near one of the two points created by the intersection of the TB and trijunction.[20,21,23,24] As shown in Figure 6b, this reduces the number of available growth directions to *two*, such that only [211] → [1$\bar{1}$2] and [12$\bar{1}$] kinks are possible, and the resulting superstructures are coherent. By virtue of the continuous TB, all segments of coherent ⟨211⟩/⟨211⟩ kinking superstructures occupy the same plane and exhibit a fixed kink angle of 120°, as previously reported.[9] We note that two $\{111\}_{SL}$ facets are theoretically possible, although energetically unfavorable, in the absence of a TB. While this situation would also break the symmetry of the growth front, prior work has shown that this solid−liquid interface is only observed in the presence of TB,[20] which is why we refer to the TB as the symmetry-breaking structural motif.

The covalent bonding of atoms to semiconductor surfaces, here hydrogen atoms on Si, modifies interface energetics[38] and likely impacts nanowire growth. Since adsorption and desorption are exponentially dependent on temperature, substantial changes can occur over a narrow range of growth conditions. Our prior *operando* infrared study of the Au/Si system, where the effects of Si_2H_6 pressure, substrate temperature, and

H atom exposure were examined in detail for ⟨111⟩ → ⟨211⟩ kinking, identified surface hydrogen's ability to modify the force balance at the trijunction.[17] The detailed crystal structure analysis and *operando* infrared data included herein for ⟨211⟩ → ⟨111⟩ or ⟨211⟩ kinking extend our previous results and provide additional evidence of surface chemistry's importance. For a ⟨211⟩ → ⟨211⟩ kink, two degenerate ⟨211⟩ segments simultaneously exist in the same nanowire. Both segments are bound by the *same* hydrogen-terminated {111} and {113} facets (Figures 5b and S3), but exhibit *distinct* liquid−solid interface geometries and thus contact angles (Figures S3, S4, and S5). The constancy of sidewall chemistry and structure during ⟨211⟩ segment growth indicates that the solid−vapor interface energy, not the liquid−solid or liquid−vapor interface energies, dominates growth direction selection. While a TB is also present in both ⟨211⟩ segments and helps to break the symmetry of the trijunction as discussed above in the context of superstructure coherence, it does not play a major role in continuous ⟨211⟩ growth. In particular, we observe that ⟨111⟩ growth returns, the TB terminates, and the solid−liquid interface flattens upon hydrogen removal. Thus, despite the favorability of nucleation at a TB when it is present,[20,24] the TB cannot in and of itself drive continuous ⟨211⟩ growth. Reports of kinked nanowires without internal defects further suggest the TB's minority role in selecting growth direction.[10,39,40] While the TB does not appear essential for continued ⟨211⟩ growth, we note that it may help overcome a kinetic barrier during the initial ⟨111⟩ → ⟨211⟩ kinking process (Figure 1). However, further studies are required to understand this effect.

CONCLUSION

We show that Si nanowire kinking superstructures comprised of ⟨211⟩ segments exhibit a continuous TB that lies in the same plane as the superstructure. We propose a mechanism by which this TB reduces the symmetry of the growth front, restricts the number of available growth directions, and results in structurally coherent ⟨211⟩/⟨211⟩ superstructures for the Au/Si system. The presence of adsorbed hydrogen atoms only during ⟨211⟩ growth, in conjunction with the observation of multiple liquid−solid interface morphologies and TB elimination for ⟨211⟩ → ⟨211⟩ and ⟨211⟩ → ⟨111⟩ kinking, respectively, further highlights the importance of solid−vapor chemical bonding. Our findings demonstrate that future attempts to engineer alternative and simultaneously highly coherent, kinking superstructures should combine (1) novel chemistries to favor different growth directions and (2) a symmetry-breaking structural feature, for example a defect, to limit the number of nucleation points.

METHODS

Si nanowires are grown on a Si (111) substrate in a custom-built ultra-high-vacuum (UHV) chamber described previously.[17] Samples are cut to 5 mm × 24 mm and precleaned in 1 M HF solution for 5 min to remove the native oxide. After deionized water rinsing for 30 s and drying with N_2, the sample is immediately loaded into the UHV chamber and heated to 700 °C for 1 h under vacuum *via* direct resistive heating. Sample temperature is monitored by an infrared pyrometer. The sample is then cleaned by annealing to 1200 °C for 30 s and cooled to room temperature at a rate below 2 °C/s. A ~2 nm thick Au film is thermally evaporated after the substrate reaches room temperature.

To simplify the identification and comparison of different growth directions, all nanowires are initiated with a [111] segment oriented perpendicular to the Si(111) substrate. This substrate-attached [111] segment is initiated at a disilane (Voltaix, Si_2H_6, 99.998%) pressure of 2×10^{-4} Torr and substrate temperature of 590 °C for 2 min before lowering the substrate temperature to 490 °C at constant Si_2H_6 pressure for an additional 10 min. The kinks of interest, specifically ⟨211⟩ → ⟨111⟩ or ⟨211⟩ → ⟨211⟩, are subsequently formed by applying the sequence of growth conditions, denoted I and II, shown in Figure 1. Condition I constitutes a Si_2H_6 pressure of 5×10^{-4} Torr and substrate temperature of 410 °C, while condition II constitutes a Si_2H_6 pressure of 2×10^{-4} Torr and substrate temperature of 490 °C. The temperature ramp rate at all condition changes is 8 °C/s for both cooling and heating.

Surface hydrogen covalently bonded to the nanowire sidewall is measured *via operando* transmission infrared spectroscopy. The FTIR spectrometer (Bruker V70) is equipped with a KBr beamsplitter and HgCdTe detector.[17] In this work, all spectra are collected with a 58° angle of incidence. All spectra consist of 1200 and 1680 scans for 5 and 7 min acquisition times, respectively, with a resolution of 4 cm^{-1}. A background scan is initially recorded upon application of condition I following growth of the substrate-attached [111] segment. A new background scan is recorded after the I → II transition (*i.e.*, for ⟨211⟩ → ⟨111⟩ kinks), due to the extended temperature change, but not the brief I → II → I transition (*i.e.*, for ⟨211⟩ → ⟨211⟩ kinks). All spectra are baseline corrected with a standard concave rubberband procedure.

Si nanowire kink morphology and crystal structure are analyzed *via* a Zeiss Ultra 60 field emission scanning electron microscope (SEM) and a FEI Titan S80-300 transmission electron microscope (TEM). Nanowires are removed from the growth substrate for TEM measurement *via* ultrasonication in 2-propanol and then drop cast onto lacey carbon grids (Ted Pella).

Conflict of Interest: The authors declare no competing financial interest.

Acknowledgment. The authors gratefully acknowledge support from the National Science Foundation (CBET #1133563). Research was supported by ORNL's Shared Research Equipment (ShaRE) User Program, which is sponsored by the Office of Basic Energy Sciences, the U.S. Department of Energy.

Supporting Information Available: Additional figures as referenced in the main text. This material is available free of charge *via* the Internet at http://pubs.acs.org.

REFERENCES AND NOTES

1. Tian, B. Z.; Cohen-Karni, T.; Qing, Q.; Duan, X. J.; Xie, P.; Lieber, C. M. Three-Dimensional, Flexible Nanoscale Field-Effect Transistors as Localized Bioprobes. *Science* **2010**, *329*, 830–834.
2. Jiang, Z.; Qing, Q.; Xie, P.; Gao, R. X.; Lieber, C. M. Kinked p-n Junction Nanowire Probes for High Spatial Resolution

Sensing and Intracellular Recording. *Nano Lett.* **2012**, *12*, 1711–1716.
3. Xu, L.; Jiang, Z.; Qing, Q.; Mai, L. Q.; Zhang, Q. J.; Lieber, C. M. Design and Synthesis of Diverse Functional Kinked Nanowire Structures for Nanoelectronic Bioprobes. *Nano Lett.* **2013**, *13*, 746–751.
4. Zhang, S.; Zhou, J.; Park, Y.-S.; Rho, J.; Singh, R.; Nam, S.; Azad, A. K.; Chen, H.-T.; Yin, X.; Taylor, A. J.; *et al.* Photoinduced Handedness Switching in Terahertz Chiral Metamolecules. *Nat. Commun.* **2012**, *3*, 942.
5. Jiang, J. W.; Yang, N.; Wang, B. S.; Rabczuk, T. Modulation of Thermal Conductivity in Kinked Silicon Nanowires: Phonon Interchanging and Pinching Effects. *Nano Lett.* **2013**, *13*, 1670–1674.
6. Jiang, J. W.; Rabczuk, T. Mechanical Oscillation of Kinked Silicon Nanowires: A Natural Nanoscale Spring. *Appl. Phys. Lett.* **2013**, *102*, 123104.
7. Pevzner, A.; Engel, Y.; Elnathan, R.; Tsukernik, A.; Barkay, Z.; Patolsky, F. Confinement-Guided Shaping of Semiconductor Nanowires and Nanoribbons: "Writing with Nanowires". *Nano Lett.* **2012**, *12*, 7–12.
8. Chen, H. A.; Wang, H.; Zhang, X. H.; Lee, C. S.; Lee, S. T. Wafer-Scale Synthesis of Single-Crystal Zigzag Silicon Nanowire Arrays with Controlled Turning Angles. *Nano Lett.* **2010**, *10*, 864–868.
9. Tian, B. Z.; Xie, P.; Kempa, T. J.; Bell, D. C.; Lieber, C. M. Single-Crystalline Kinked Semiconductor Nanowire Superstructures. *Nat. Nanotechnol.* **2009**, *4*, 824–829.
10. Musin, I. R.; Filler, M. A. Chemical Control of Semiconductor Nanowire Kinking and Superstructure. *Nano Lett.* **2012**, *12*, 3363–3368.
11. Cohen-Karni, T.; Casanova, D.; Cahoon, J. F.; Qing, Q.; Bell, D. C.; Lieber, C. M. Synthetically Encoded Ultrashort-Channel Nanowire Transistors for Fast, Pointlike Cellular Signal Detection. *Nano Lett.* **2012**, *12*, 2639–2644.
12. Lauhon, L. J.; Gudiksen, M. S.; Wang, D.; Lieber, C. M. Epitaxial Core-Shell and Core-Multishell Nanowire Heterostructures. *Nature* **2002**, *420*, 57–61.
13. Madras, P.; Dailey, E.; Drucker, J. Kinetically Induced Kinking of Vapor-Liquid-Solid Grown Epitaxial Si Nanowires. *Nano Lett.* **2009**, *9*, 3826–3830.
14. Madras, P.; Dailey, E.; Drucker, J. Spreading of Liquid AuSi on Vapor-Liquid-Solid Grown Si Nanowires. *Nano Lett.* **2010**, *10*, 1759–1763.
15. Lugstein, A.; Steinmair, M.; Hyun, Y. J.; Hauer, G.; Pongratz, P.; Bertagnolli, E. Pressure-Induced Orientation Control of the Growth of Epitaxial Silicon Nanowires. *Nano Lett.* **2008**, *8*, 2310–2314.
16. Dailey, E.; Madras, P.; Drucker, J. Composition and Growth Direction Control of Epitaxial Vapor-Liquid-Solid-Grown SiGe Nanowires. *Appl. Phys. Lett.* **2010**, *97*, 143106.
17. Shin, N.; Filler, M. A. Controlling Silicon Nanowire Growth Direction *via* Surface Chemistry. *Nano Lett.* **2012**, *12*, 2865–2870.
18. Wang, J.; Plissard, S. R.; Verheijen, M. A.; Feiner, L. F.; Cavalli, A.; Bakkers, E. Reversible Switching of InP Nanowire Growth Direction by Catalyst Engineering. *Nano Lett.* **2013**, *13*, 3802–3806.
19. Davidson, F. M.; Lee, D. C.; Fanfair, D. D.; Korgel, B. A. Lamellar Twinning in Semiconductor Nanowires. *J. Phys. Chem. C* **2007**, *111*, 2929–2935.
20. Dayeh, S. A.; Wang, J.; Li, N.; Huang, J. Y.; Gin, A. V.; Picraux, S. T. Growth, Defect Formation, and Morphology Control of Germanium-Silicon Semiconductor Nanowire Heterostructures. *Nano Lett.* **2011**, *11*, 4200–4206.
21. Dayeh, S. A.; Liu, X. H.; Dai, X.; Huang, J. Y.; Picraux, S. T.; Soci, C. Rocking Chair Defect Generation in Nanowire Growth. *Appl. Phys. Lett.* **2012**, *101*, 053121.
22. Lopez, F. J.; Givan, U.; Connell, J. G.; Lauhon, L. J. Silicon Nanowire Polytypes: Identification by Raman Spectroscopy, Generation Mechanism, and Misfit Strain in Homostructures. *ACS Nano* **2011**, *5*, 8958–8966.
23. Jeon, N.; Dayeh, S. A.; Lauhon, L. J. Origin of Polytype Formation in VLS-Grown Ge Nanowires through Defect Generation and Nanowire Kinking. *Nano Lett.* **2013**, *13*, 3947–3952.
24. Tang, W.; Picraux, S. T.; Huang, J. Y.; Gusak, A. M.; Tu, K. N.; Dayeh, S. A. Nucleation and Atomic Layer Reaction in Nickel Silicide for Defect-Engineered Si Nanochannels. *Nano Lett.* **2013**, *13*, 2748–2753.
25. Dailey, E.; Madras, P.; Drucker, J. Au on Vapor-Liquid-Solid Grown Si Nanowires: Spreading of Liquid AuSi from the Catalytic Seed. *J. Appl. Phys.* **2010**, *108*, 064320.
26. Kempa, T. J.; Kim, S.-K.; Day, R. W.; Park, H.-G.; Nocera, D. G.; Lieber, C. M. Facet-Selective Growth on Nanowires Yields Multi-Component Nanostructures and Photonic Devices. *J. Am. Chem. Soc.* **2013**, *135*, 18354–18357.
27. Hyun, Y.-J.; Lugstein, A.; Steinmair, M.; Bertagnolli, E.; Pongratz, P. Orientation Specific Synthesis of Kinked Silicon Nanowires Grown by the Vapour-Liquid-Solid Mechanism. *Nanotechnology* **2009**, *20*, 125606.
28. Cayron, C.; Den Hertog, M.; Latu-Romain, L.; Mouchet, C.; Secouard, C.; Rouviere, J. L.; Rouviere, E.; Simonato, J. P. Odd Electron Diffraction Patterns in Silicon Nanowires and Silicon Thin Films Explained by Microtwins and Nanotwins. *J. Appl. Crystallogr.* **2009**, *42*, 242–252.
29. Kohno, H.; Ozaki, N.; Yoshida, H.; Tanaka, K.; Takeda, S. Misleading Fringes in TEM Images and Diffraction Patterns of Si Nanocrystallites. *Cryst. Res. Technol.* **2003**, *38*, 1082–1086.
30. Fontcuberta i Morral, A.; Arbiol, J.; Prades, J. D.; Cirera, A.; Morante, J. R. Synthesis of Silicon Nanowires with Wurtzite Crystalline Structure by Using Standard Chemical Vapor Deposition. *Adv. Mater.* **2007**, *19*, 1347–1351.
31. Fabbri, F.; Rotunno, E.; Lazzarini, L.; Cavalcoli, D.; Castaldini, A.; Fukata, N.; Sato, K.; Salviati, G.; Cavallini, A. Preparing the Way for Doping Wurtzite Silicon Nanowires while Retaining the Phase. *Nano Lett.* **2013**, *13*, 5900–5906.
32. den Hertog, M. I.; Cayron, C.; Gentile, P.; Dhalluin, F.; Oehler, F.; Baron, T.; Rouviere, J. L. Hidden Defects in Silicon Nanowires. *Nanotechnology* **2012**, *23*, 025701.
33. Uccelli, E.; Arbiol, J.; Magen, C.; Krogstrup, P.; Russo-Averchi, E.; Heiss, M.; Mugny, G.; Morier-Genoud, F.; Nygard, J.; Morante, J. R.; *et al.* Three-Dimensional Multiple-Order Twinning of Self-Catalyzed GaAs Nanowires on Si Substrates. *Nano Lett.* **2011**, *11*, 3827–3832.
34. Gupta, P.; Colvin, V. L.; George, S. M. Hydrogen Desorption-Kinetics from Monohydride and Dihydride Species on Silicon Surfaces. *Phys. Rev. B* **1988**, *37*, 8234–8243.
35. Hillerich, K.; Dick, K. A.; Wen, C. Y.; Reuter, M. C.; Kodambaka, S.; Ross, F. M. Strategies to Control Morphology in Hybrid Group III−V/Group IV Heterostructure Nanowires. *Nano Lett.* **2013**, *13*, 903–908.
36. Wen, C. Y.; Tersoff, J.; Hillerich, K.; Reuter, M. C.; Park, J. H.; Kodambaka, S.; Stach, E. A.; Ross, F. M. Periodically Changing Morphology of the Growth Interface in Si, Ge, and GaP Nanowires. *Phys. Rev. Lett.* **2011**, *107*, 025503.
37. Gamalski, A. D.; Ducati, C.; Hofmann, S. Cyclic Supersaturation and Triple Phase Boundary Dynamics in Germanium Nanowire Growth. *J. Phys. Chem. C* **2011**, *115*, 4413–4417.
38. Stekolnikov, A. A.; Furthmuller, J.; Bechstedt, F. Absolute Surface Energies of Group-IV Semiconductors: Dependence on Orientation and Reconstruction. *Phys. Rev. B* **2002**, *65*, 115318.
39. Meister, S.; Peng, H. L.; McIlwrath, K.; Jarausch, K.; Zhang, X. F.; Cui, Y. Synthesis and Characterization of Phase-Change Nanowires. *Nano Lett.* **2006**, *6*, 1514–1517.
40. Jung, C. S.; Kim, H. S.; Im, H. S.; Seo, Y. S.; Park, K.; Back, S. H.; Cho, Y. J.; Kim, C. H.; Park, J.; Ahn, J. P. Polymorphism of GeSbTe Superlattice Nanowires. *Nano Lett.* **2013**, *13*, 543–549.